I&EC research
Industrial & Engineering Chemistry Research

pubs.acs.org/IECR

Article

Development of a Filtered CFD-DEM Drag Model with Multiscale Markers Using an Artificial Neural Network and Nonlinear Regression

Liqiang Lu,* Xi Gao, Jean-François Dietiker, Mehrdad Shahnam, and William A. Rogers

Cite This: *Ind. Eng. Chem. Res.* 2022, 61, 882−893

Read Online

ACCESS | Metrics & More | Article Recommendations

ABSTRACT: The accuracy of coarse-grained Euler−Lagrangian simulations of fluidized beds heavily depends on the mesoscale drag models to account for the influences of the unresolved subgrid structures. Traditional filtered drag models are regressed with mesoscale markers such as voidage and slip velocities. In this research, a filtered drag was regressed with both mesoscale and macroscale markers using fine-grid Computational Fluid Dynamics−Discrete Element Method (CFD-DEM) simulations. The traditional nonlinear regression method was compared with machine learning regression using an Artificial Neural Network (ANN) implemented in PyTorch and coupled with MFiX. The new drag showed higher accuracy than the Wen−Yu drag and another filtered drag derived from the two-fluid model. The nonlinear regression shows slightly better results than ANN regression in cases with similar R^2 values. The utilization of the gas inlet velocity as an additional macroscale marker reduced the errors by up to 55.3% in the tested cases.

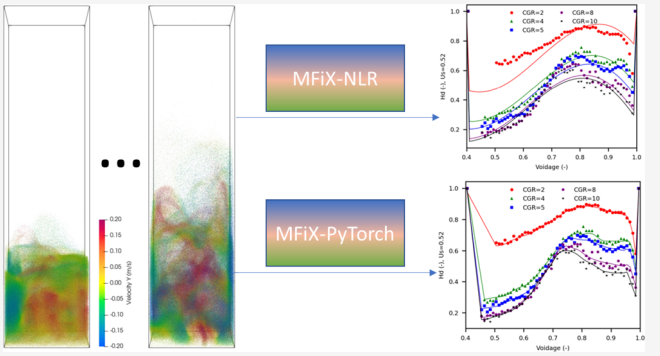

1. INTRODUCTION

Fluidized beds are widely used in biomass pyrolysis and gasification,[1,2] methanol-to-olefins,[3−5] coal gasification,[6] and many other processes that need good gas−solids mixing. The strong gas−solids interactions lead to complex hydrodynamic phenomena including bubbling, slugging, clustering, and channel flows.[7−9] Computational Fluid Dynamics (CFD) simulations with the fine-grid two-fluid model (TFM) can capture these complex phenomena.[10] However, they are not suitable for practical use at large scales due to the large computation cost. Coarse-grid simulations with mesoscale drag corrections are widely used in practice.[5,11−14] The mesoscale drag models such as the Energy Minimization Multi-Scale (EMMS) drag and the filtered drag greatly improved the accuracy of the coarse-grid simulations.[15,16] The recently developed spatially averaged TFM can also predict accurate results using coarse CFD grids with constitutive relations derived from fine-grid TFM simulations.[17−19] These models considerably enhanced the utilization of CFD in the simulation of fluidized beds.

In the EMMS model, the drag coefficient is obtained by solving a nonlinear optimization problem constructed from the lumped hydrodynamic equations closed by a stability condition. In an early study,[20] the EMMS drag model was derived by adding an acceleration term. The drag model was regressed as a function of voidage. Then it was further developed by considering the different acceleration velocities of the dilute phase and dense phase.[21,22] The drag was regressed as a function of voidage and slip velocity. Later, a revised cluster size model extended the applicability of the EMMS drag to both Geldart A and Geldart B particles.[23] The bubble-based EMMS model extended its applicability to bubbling and turbulent fluidization regimes.[24−26] Further research includes the extension to binary systems[12,27] and the coupling with Euler−Lagrangian simulations.[28−30] Recently, a generic EMMS drag model was developed using an Artificial Neural Network (ANN) to cover a wide range of material properties and operating conditions.[31,32]

In the filtered model, the drag coefficient is obtained by filtering fine-grid simulations. In the early study,[33,34] the filtered drag was regressed as a function of voidage. Further developments added the slip velocity,[35−37] voidage gradient,[38] and material properties[39] to the regression model. The drag coefficient was also modeled with a drift velocity[40−42] that is defined as the difference between the filtered gas velocity seen by

Received: September 9, 2021
Revised: November 26, 2021
Accepted: November 30, 2021
Published: December 26, 2021

https://doi.org/10.1021/acs.iecr.1c03644
Ind. Eng. Chem. Res. 2022, 61, 882−893

the particle phase and the filtered gas velocity seen by the gas phase. The drift velocity was regressed as a function of voidage, slip velocity, and other case-dependent parameters. Recently, the ANN-based regression showed better correction coefficients than nonlinear regressions. It was used to regress filtered drag using pressure gradients as an additional maker,[43,44] considering the influence of neighboring cells,[45] and generalization with different material properties and cascading-based extrapolation to larger filter size.[46]

The current filtered drag models only used mesoscale markers without considering the effect of macroscale markers that are commonly used in the EMMS drag. Fundamentally, there are no macroscale parameters in the volume-averaged Navier−Stokes equations. However, these equations are subject to boundary conditions, which are macroscale parameters, e.g., inlet velocity. The influences of macroscale parameters over the filtered drag and stress models of gas−solid flows were reported in the literature. The simulation of riser flows showed that the effective drag is significantly influenced by both gas velocity and solid hold-up.[47] The macroscale domain averaged Reynolds number and solid fractions were found to have a substantial effect on filtered and residual stress.[48]

TFM simulations have difficulties resolving particle size distributions (PSDs) and capturing the influence of particle shapes, while the Euler−Lagrangian methods can directly resolve them.[49] Current research indicates that the subgrid drag models are also important to the coarse-grained Euler−Lagrangian simulations.[29,50−52] Similar to the filtering of fine-grid TFM, the filtered drag model can also be constructed from the filtering of fine-grid CFD-DEM simulations.[53−55] The subgrid gas velocity was also reconstructed from the grid-scale pressure balance equation according to weighted local porosities[56] or simplified momentum equations.[54] However, due to the limited research of filtered CFD-DEM drag models, many of the coarse-grained Euler−Lagrangian simulations are still using the drag models derived from fine-grid TFM.[51,57,58] Recent research[59] showed that the filtered TFM drag model overcorrects the influence of subgrid structures if used for simulations with only fluid coarse-graining.

This research will derive a mesoscale drag correction through the filtering of fine-grid CFD-DEM simulations of a fluidized bed under different superficial gas velocities. The macroscale gas velocity and mesoscale voidage and slip velocity will be used as regression markers. The ANN and traditional nonlinear regression methods will be compared. Lastly, the filtered drag for coarse-grained CFD-DEM simulations will be tested in the simulation of a bubbling fluidized bed with different operating conditions.

2. METHOD

2.1. The Gas Phase Model. In Euler−Lagrangian simulations, the gas phase is governed by volume-averaged Navier−Stokes equations:

$$\frac{\partial(\varepsilon_g\rho_g)}{\partial t} + \nabla\cdot(\varepsilon_g\rho_g\mathbf{u}_g) = 0 \tag{1}$$

$$\frac{\partial(\varepsilon_g\rho_g\mathbf{u}_g)}{\partial t} + \nabla\cdot(\varepsilon_g\rho_g\mathbf{u}_g\mathbf{u}_g) = -\varepsilon_g\nabla P + \varepsilon_g\nabla\cdot\tau_g + \varepsilon_g\rho_g\mathbf{g} - \mathbf{I}_{drag} \tag{2}$$

where ε_g, ρ_g, and $\mathbf{u}_g$are the volume fraction, density, and velocity of the gas phase; P_g is the pressure for the gas phase; and $\boldsymbol{\tau}_g$is the stress for the gas phase. $\mathbf{g}$ is gravity and $\mathbf{I}_{drag}$is the gas−solid drag force.

2.2. The Solid Phase Model. The movements of the particles are based on Newton's second law of motion:

$$m_p\frac{d\mathbf{v}_p}{dt} = m_p\mathbf{g} - \frac{\pi}{6}d_p^3\nabla P_g + \frac{\beta(\mathbf{u}_g(\mathbf{x}^i) - \mathbf{v}_p)}{1-\varepsilon_g}\frac{\pi}{6}d_p^3 + \mathbf{F}_C \tag{3}$$

where m_p is the mass of the particle and d_p is its diameter. $\mathbf{v}_p$ is the translation velocity of the particle. The forces considered include the gravity force, pressure gradient force, drag force, and collision force ($\mathbf{F}_C$). The drag coefficient β is calculated using the Wen−Yu drag model. The collision force is calculated by the linear spring-dashpot model in DEM:

$$\mathbf{F}_c = \mathbf{F}_c^n + \mathbf{F}_c^t \tag{4}$$

$$\mathbf{F}_c^n = -k_n\delta_n\mathbf{n} - \eta_n\mathbf{v}_n \tag{5}$$

$$\mathbf{F}_c^t = \min\left(-k_t\boldsymbol{\delta}_t - \eta_t\mathbf{v}_t, \mu_s|\mathbf{F}_c^n|\frac{\boldsymbol{\delta}_t}{|\boldsymbol{\delta}_t|}\right) \tag{6}$$

where $\mathbf{n}$ is the unit vector in the normal direction. k_n and k_t are spring constants in normal and tangential directions, respectively. η_n and η_t are damping coefficients in normal and tangential directions, respectively. δ_n is the particle−particle overlap. $\mathbf{v}_n$ and $\mathbf{v}_t$ are relative velocities in normal and tangential directions. μ_s is the sliding friction. $\boldsymbol{\delta}_t^{(n)}$ and $\boldsymbol{\delta}_t^{(n-1)}$ are the tangential overlap at the current and the previous step.

The rotations of particles are tracked by

$$I_p\frac{d\mathbf{w}_p}{dt} = \mathbf{F}_c^t \times (\mathbf{x}_c - \mathbf{x}_p) \tag{7}$$

and $\mathbf{w}_p$ is the angular velocity. The moment of inertia I_p is calculated by $m_p{d_p}^2/10$. $\mathbf{X}_c$ and $\mathbf{X}_p$ are the contact point and positions of the particle.

2.3. Estimation of Mesoscale Drag. The filtering method is illustrated in Figure 1 with an example of 16 fine grids in 2-D.

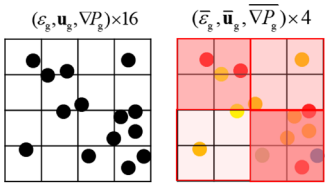

Figure 1. The filtering of fine-grid CFD-DEM simulations (a) with a coarse-graining ratio of 2 (b). The colors of particles represent the different heterogeneous indexes.

The filtering of the fine-grid simulation is the coarse-graining of the gas phase variables. As shown in Figure 1, considering a domain with 16 fine grids, the coarse-graining with a ratio of 2 lumps them into four coarse grids. The values of the coarse-grained voidage ($\overline{\varepsilon}_g$), velocity ($\overline{\mathbf{u}}_g$), and pressure gradient ($\overline{\nabla P_g}$) are calculated by

$$\overline{\varepsilon}_g = \sum_{i=1}^{N}\frac{\varepsilon_{g,i}}{N} \tag{8}$$

https://doi.org/10.1021/acs.iecr.1c03644
Ind. Eng. Chem. Res. 2022, 61, 882−893

$$\bar{\mathbf{u}}_g = \sum_{i=1}^{N} \frac{\mathbf{u}_{g,i}\varepsilon_{g,i}}{N\bar{\varepsilon}_g} \tag{9}$$

$$\overline{\nabla P_g} = \sum_{i=1}^{N} \frac{\nabla P_{g,i}\varepsilon_{g,i}}{N\bar{\varepsilon}_g} \tag{10}$$

where N is the number of fine grids lumped into a coarse grid.

The interphase force per particle volume is a summarization of the pressure gradient force and the drag force. In the fine-grid simulation, it is calculated as

$$\mathbf{f}_{\text{fineGrid}}^{\text{particle},i} = -\nabla P_g + \frac{\beta_{\text{fineGrid}}^{\text{WenYu}}}{1-\varepsilon_g}(\mathbf{u}_g - \mathbf{v}_p^{\text{particle},i}) \tag{11}$$

where $\beta_{\text{fineGrid}}^{\text{WenYu}}$ is the drag coefficient calculated with the Wen−Yu drag[60] model.

After coarse-graining of the CFD grids, this force is expressed as

$$\mathbf{f}_{\text{coarseGrid}}^{\text{particle},i} = -\overline{\nabla P_g} + \frac{\beta_{\text{coarseGrid}}}{1-\bar{\varepsilon}_g}(\bar{\mathbf{u}}_g - \mathbf{v}_p^{\text{particle},i}) \tag{12}$$

$$\beta_{\text{coarseGrid}} = H_d \beta_{\text{coarseGrid}}^{\text{WenYu}} \tag{13}$$

The heterogeneous index H_d is introduced to address the influence of coarse-graining. Letting $\mathbf{f}_{\text{coarseGrid}}^{\text{particle},i}$ be equal to $\mathbf{f}_{\text{fineGrid}}^{\text{particle},i}$, we can get

$$H_d = \frac{\left(\overline{\nabla P_g} - \nabla P_g + \frac{\beta_{\text{fineGrid}}^{\text{WenYu}}}{1-\varepsilon_g}(\mathbf{u}_g - \mathbf{v}_p^{\text{particle},i})\right)}{\beta_{\text{coarseGrid}}^{\text{WenYu}}(\bar{\mathbf{u}}_g - \mathbf{v}_p^{\text{particle},i})}(1-\bar{\varepsilon}_g) \tag{14}$$

H_d is calculated for each particle in the system. In this process, the effect of pressure gradient force is lumped with drag force as the same simplification was used in previous research due to its minor effect.[51,53] The influence of particle coarse-graining was also neglected as its effect was reported as minor in a previous research.[51] However, the generated model was tested with both fluid coarse-graining and particle coarse-graining in this research.

2.4. Coupling MFiX with PyTorch. In this research, the filtered drag was regressed with both traditional nonlinear regression (NLR) and artificial neural network (ANN) implemented in PyTorch (https://pytorch.org/). The NLR-based model was coupled with MFiX by explicit implementation in the MFiX *usr_drag* module. As illustrated in Figure 2, the Fortran-based MFiX and Python-based PyTorch model was coupled through Fortran-Call-C and PyTorch C++ API (LibTorch). The PyTorch model was converted to Torch Script via tracing. Then, the Torch Script was serialized and saved to a file that was then loaded with the MFiX-PyTorch program at runtime. A demo case is available to share upon reasonable request.

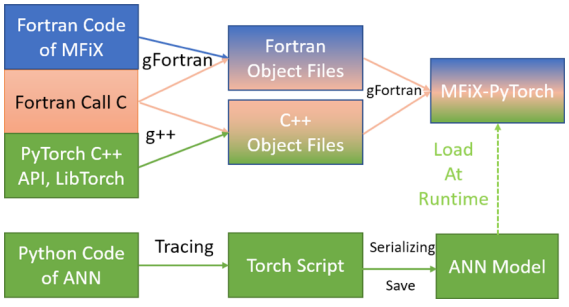

Figure 2. Flowchart illustrating the coupling of MFiX and PyTorch-based ANN model.

2.5. Fine-Grid CFD-DEM Simulations. The air fluidization of Geldart A particles with a diameter of 0.075 mm and a density of 1500 kg/m^3 was simulated with MFiX-DEM with parameters in Table 1. As shown in Figure 3, the rectangular fluidized bed has a cross section of 120 d_p × 120 d_p and a height of 480 d_p. The particles are initialized at the bottom section with a height of 120 d_p and a voidage of 0.6. The CFD grid size is 3 d_p in each direction, and the Divide Particle Volume Method (DPVM) is used to calculate the interphase interpolations. The gas flows into the bed from the bottom boundary with a constant velocity and flows out from the top boundary with a constant pressure of 101.3 kPa. Nonslip boundary conditions are used at four sidewalls. Configuration of this fluidized bed was also used in other researches investigating subgrid drag corrections.[43,59]

Table 1. Particle Properties and Parameters Used in the Fine-Grid CFD-DEM Simulations

properties/parameters	value
particle diameter (mm)	0.075
particle density (kg/m^3)	1500
spring constant (N/m)	10
restitution coefficient (−)	0.9
friction coefficient (−)	0.3
inlet gas velocity (m/s)	0.050, 0.075, 0.100, 0.125, 0.150

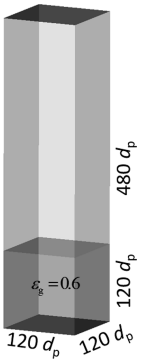

Figure 3. Dimensions of the simulated fluidized bed.

3. RESULTS

3.1. Filtered Drag from Bubbling Bed with One Macroscale Velocity. In this section, the fluidized bed in Figure 3 was simulated with a gas inlet velocity of 0.10 m/s. There are 1.32 million particles in the fluidized bed. The results from 3.0 to 7.0 s were analyzed at a frequency of 20 Hz. The total number of particle data points is about 104 million.

3.1.1. Regression of Mesoscale Drag. Considering different coarse-graining ratios, the total number of H_d counts can be billions. To reduce the difficulties in data processing and also avoid the influence of noise, the results of H_d are binned based on the filtered voidage and dimensionless filtered slip velocity calculated as

https://doi.org/10.1021/acs.iecr.1c03644
Ind. Eng. Chem. Res. 2022, 61, 882−893

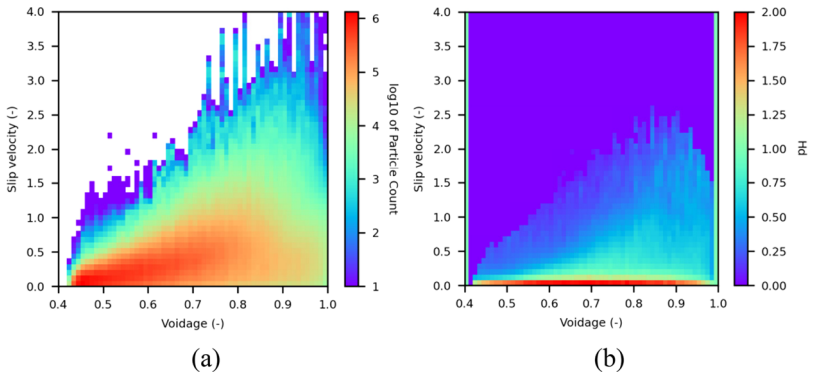

Figure 4. Heat map of filtered voidage and dimensionless slip velocity with a coarse-graining ratio of 5 generated from fine-grid CFD-DEM simulation (a) and binned results of the heterogeneous index (b).

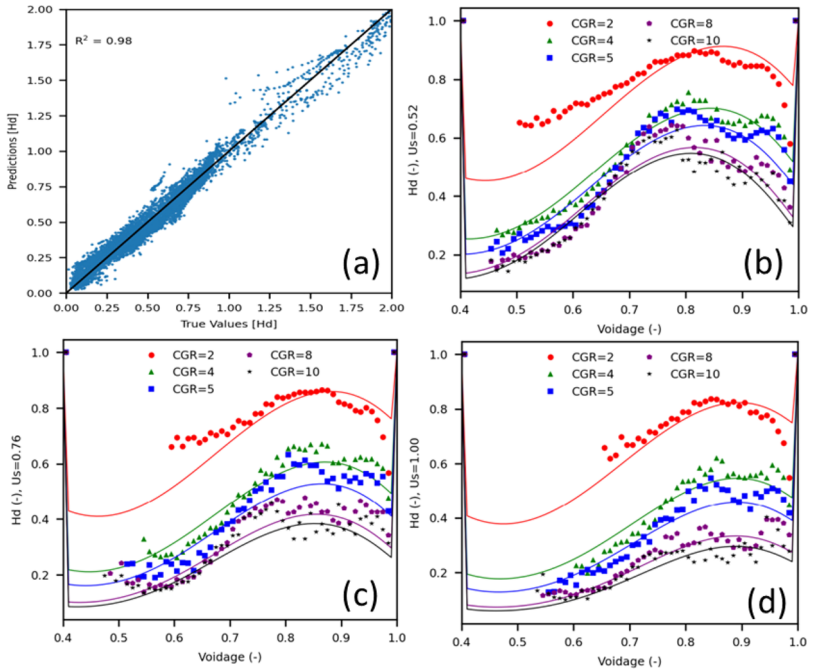

Figure 5. Comparison between true values and NLR regression predicted values of the heterogeneous index. (a) Plot of true values and predicted values. (b, c, and d) Results at different coarse-graining ratios (CGRs) and dimensionless slip velocities of 0.52, 0.76, and 1.00, respectively. Scatter points: true values, lines: regressed values.

$$u_{\text{slip}}^{*} = \frac{u_{\text{slip}}}{u_{\text{t}}} \tag{15}$$

$$u_{\text{slip}} = |\bar{\mathbf{u}}_{\text{g}} - \mathbf{v}_{\text{p}}| \tag{16}$$

$$u_{\text{t}} = \frac{g{d_{\text{p}}}^{2}(\rho_{\text{p}} - \rho_{\text{g}})}{18\mu_{\text{g}}} \tag{17}$$

where u_{t} is particle terminal velocity. These dimensionless parameters allow the model to be used for other simulations of particles with different densities and sizes.

For a coarse-graining ratio of 5, the heat map of the number of particles in terms of different filtered voidage and dimensionless slip velocities is shown in Figure 4a. The results indicated that most of the particles are in the dense region with a voidage of 0.5 to 0.6 and a dimensionless slip velocity less than 0.5. There are no particles in the region with high slip velocity and small voidage. The binned results of the heterogeneous index with a coarse-graining ratio of 5 are shown in Figure 4b. A total of 60 bins are used for filtered voidage and 50 bins are used for dimensionless filtered slip velocity. The bins with less than 1000 particles are removed from the results to avoid the influence of rare scenarios. The values at the dense bins with a voidage of 0.40 to 0.41 and the dilute bins with a voidage of 0.99 to 1.0 are set to 1.

When the slip velocity is close to 0 as shown in Figure 4b, the heterogeneous index is larger than 1. This is because, under this low slip condition, the calculated drag coefficient is very small. However, this low slip velocity is only an averaged value of many subcells with varied slip velocities and a large drag coefficient can exist in these subcells. So, the heterogeneous index is larger than 1 under these conditions. A heterogeneous index larger than 1 was also reported in a recent study to build a filtered drag model from TFM simulations.[44]

In some research,[45,54] the original data are directly used. However, there is no fundamental difference between the binned data and the original data. The binning process smoothed the numerical noise and averaged the influence of

https://doi.org/10.1021/acs.iecr.1c03644
Ind. Eng. Chem. Res. 2022, 61, 882−893

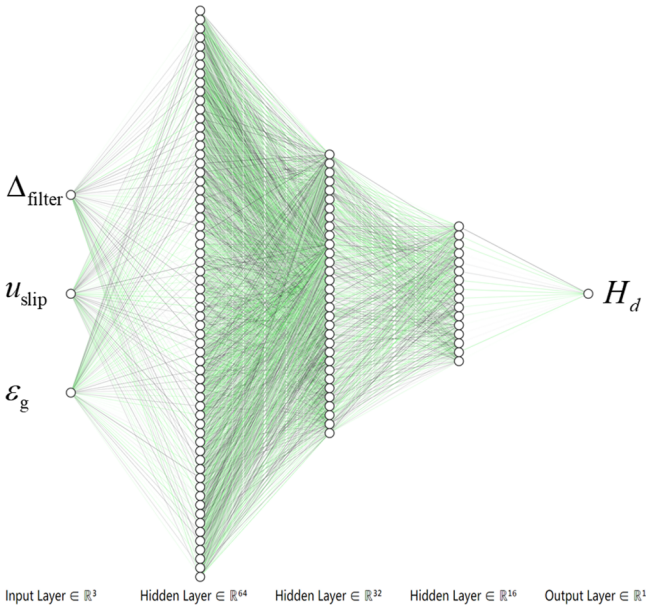

Figure 6. Structure of the artificial neural network used in this research. Three hidden layers with 64, 32, and 16 nodes.

other potential markers not included in the regression model, e.g., pressure gradient, voidage gradient, slip velocity gradient, collision forces, neighbor particles, and others. The process also eliminated the influence of different data concentrations as shown in Figure 4a where the particle count density is 6 orders of difference in different conditions. Thus, better regression coefficients are usually achieved using binned data.

Considering different filtering sizes (coarse-graining ratios), the heterogeneous index was regressed with the following equations:

$$\Delta_{filter} = 2 \times V_{cell}^{1/3} \tag{18}$$

$$\Delta^*_{filter} = \frac{2g\Delta_{filter}}{u_t^2} \tag{19}$$

$$H_d = \begin{cases} 2 - 1.99(1 - e^{-\alpha(u^*_{slip} - u_0)^p}), & u^*_{slip} > u_0 \\ 1, & u^*_{slip} \le u_0,\ \alpha_s > 0.59,\ \alpha_s < 0.01 \end{cases} \tag{20}$$

$$\alpha = \frac{(a_1 + a_2\alpha_s + a_3\alpha_s^2 + a_4\alpha_s^3 + a_5\alpha_s^4)(1 - e^{a_{19}\alpha_s})}{1 + e^{a_{20}(\alpha_s - 0.55)}} \left(1 + \frac{a_6}{\Delta^*_{filter}} + \frac{a_7}{(\Delta^*_{filter})^2}\right)\left(1 + \frac{a_8}{(v^*_{slip})^2}\right) \tag{21}$$

$$u_0 = \frac{a_9 + a_{10}\alpha_s}{0.01 + \alpha_s^{a_{11}}}\left(1 + \frac{a_{12}}{\Delta^*_{filter}} + \frac{a_{13}}{(\Delta^*_{filter})^2}\right) \tag{22}$$

$$p = (a_{14} + a_{15}\alpha_s + a_{16}\alpha_s^2)\left(1 + \frac{a_{17}}{\Delta^*_{filter}} + \frac{a_{18}}{(\Delta^*_{filter})^2}\right) \tag{23}$$

where V_{cell} is the volume of the CFD cell and $\alpha_s$is the solid volume fraction in that cell. This regression model is a modified version of the previously used model in the regression of the filtered drag derived from fine-grid TFM simulations.[37]

Using *optimize.least_squares* from *scipy*, the calculated coefficients are

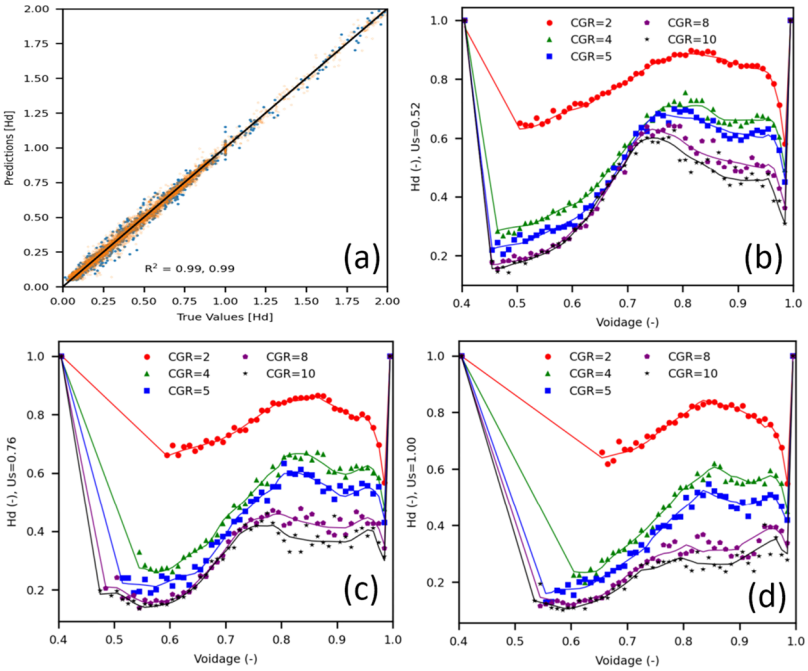

Figure 7. Comparison between true values and ANN regression predicted values of the heterogeneous index. (a) Plot of true values and predicted values. (b, c, and d) Results at different coarse-graining ratios (CGRs) and dimensionless slip velocities of 0.52, 0.76, and 1.00, respectively. Scatter points: true values, lines: regressed values.

https://doi.org/10.1021/acs.iecr.1c03644
Ind. Eng. Chem. Res. 2022, 61, 882−893

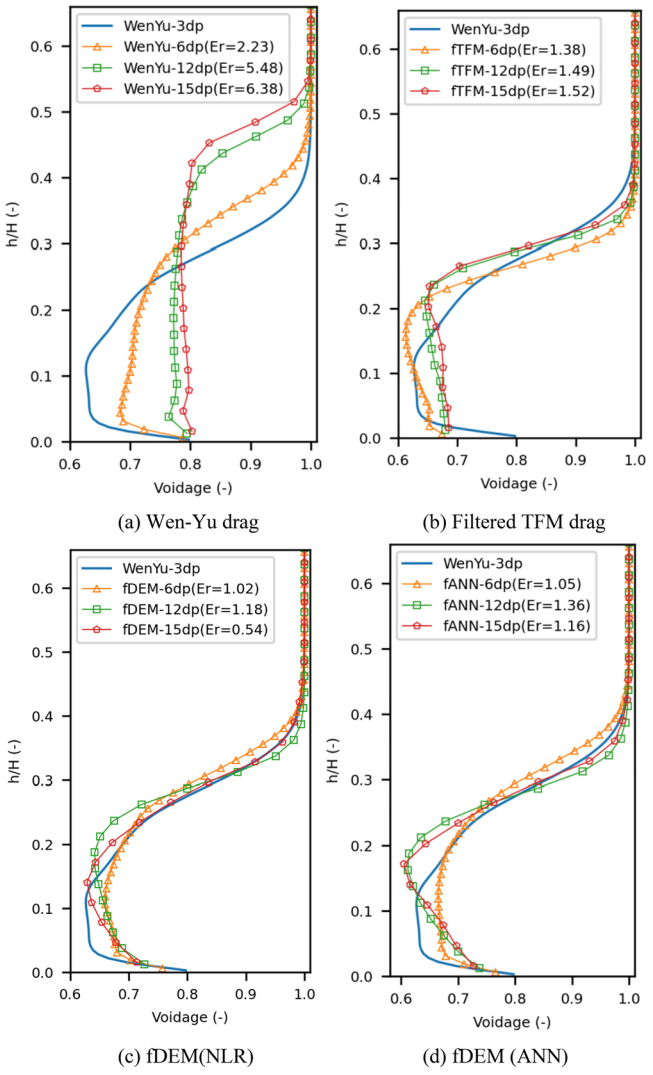

Figure 8. Voidage profiles across the height of the fluidized bed calculated with different drag models and coarse-graining ratios. 3dp, 6dp, 12dp, and 15dp in the legend indicate the CFD cell size. See eq 23 for the definition of Er.

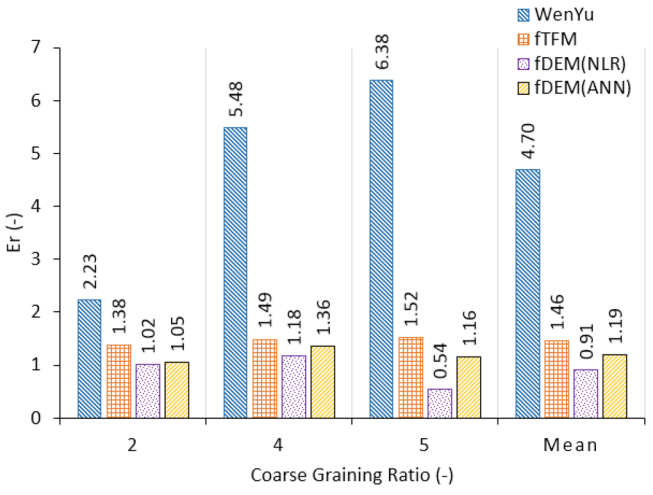

Figure 9. Relative errors of voidage profiles calculated with different drag models and coarse-graining ratios. See eq 23 for the definition of Er.

$$a_{1-20} = [2.889293, -6.932095, 42.761255, -66.421976, 93.453422, 0.011645, -0.173643, -0.001017, 1.316444, -2.480063, -2.015949, -0.055423, -0.010971, 0.162687, 5.494185, -8.473600, 0.014855, -0.209386, -693.731678, 9.931207]$$

The true values and the nonlinear regression predicted values of the heterogeneous index are compared in Figure 5a. The fitting is good as the R^2 value is 0.98 and the errors are not biased. Regressed results and true values at different coarse-graining ratios (CGRs) and dimensionless slip velocities of 0.52, 0.76, and 1.00 are compared in Figure 5b,c,d, respectively.

To further improve the regression accuracy, the same data were also regressed with an ANN implemented in PyTorch. The structure of the ANN is shown in Figure 6.

To avoid overfitting, 80% of the data was used to train the model and 20% was reserved for testing. The true values and the ANN regression predicted values of the heterogeneous index are compared in Figure 7a. The fitting is slightly better than the nonlinear regression as the R^2 value is 0.99 on both the training data and the testing data and the errors are not biased. Comparing Figure 7b,c,d with Figure 5, we can see that the traditional nonlinear regression model predicted heterogeneous index is smoother than that regressed with ANN. This is because the traditional nonlinear regression is based on a preselected form of nonlinear equation with only 20 parameters. However, the ANN used in this research has 2881 free parameters.

3.1.2. Test of the Regressed Model. To assess the performance of the regressed model, the bubbling fluidized bed was simulated with different coarse-graining ratios of 2 (6dp), 4 (12dp), and 5 (15dp). In each case, both the CFD grid size and the parcel size are scaled by the coarse-graining ratios of 2, 4, and 5. The time-averaged axial voidage profiles are compared in Figure 8. As shown in Figure 8a, the simulation with the homogeneous Wen−Yu drag model[60] predicted a higher bed height, and the relative errors increased with the increase of coarse-graining ratios. Figure 8b shows the results of CFD-DEM simulations with a filtered drag model derived from fine-grid TFM simulations.[37] The accuracies of all the tested coarse-graining ratios are significantly improved. The predicted bed height is slightly lower than the fine-grid simulation result. Figure 8c,d displays the profiles calculated with the newly derived drag model regressed with the traditional nonlinear regression (NLR) and ANN, respectively. Both of them largely increased the accuracy, and the result with the ANN regressed model does not show superiority compared with traditional NLR.

To quantify the accuracy of different simulations, the relative error is defined as

$$\mathrm{Er} = 100 \times \sum_{i=1}^{N} \frac{|\varepsilon_i^{\mathrm{CG}} - \varepsilon_i^{\mathrm{FG}}|}{N} \tag{24}$$

where N is the number of coarse CFD grids in the height direction. $\varepsilon_i^{\mathrm{CG}}$ is the averaged voidage of coarse-grained simulations. $\varepsilon_i^{\mathrm{FG}}$ is the averaged voidage of fine-grid simulations mapped to the coarse grid. Quantitative comparisons of different drag models with different coarse-graining ratios (CGRs) are shown in Figure 9. The fTFM drag, NLR-based fDEM drag, and

https://doi.org/10.1021/acs.iecr.1c03644
Ind. Eng. Chem. Res. 2022, 61, 882−893

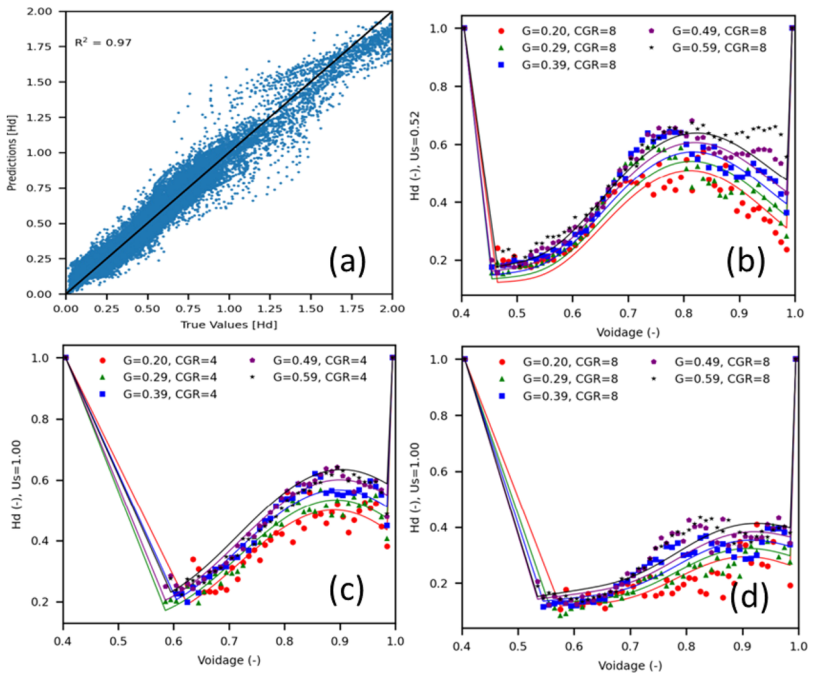

Figure 10. Comparison between true values and regression predicted values of the heterogeneous index. G: dimensionless inlet gas velocity. CGR: coarse-graining ratio. (a) Parity plot; (b) dimensionless slip velocity equals 0.52, CGR = 8; (c) dimensionless slip velocity equals 1.00, CGR = 4; and (d) dimensionless slip velocity equals 1.00, CGR = 8.

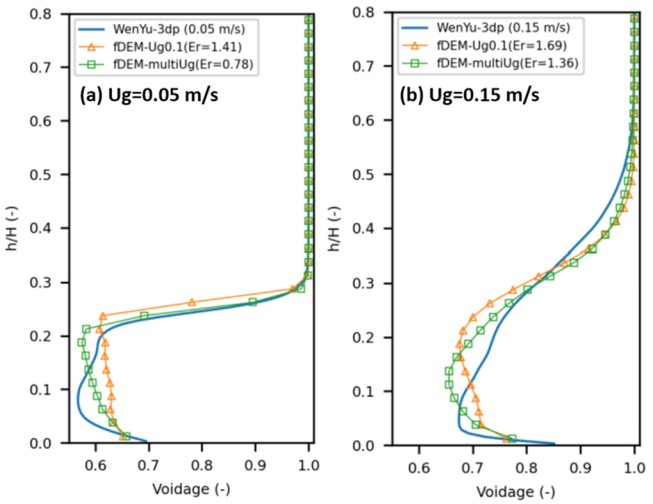

Figure 11. Voidage profiles across the height of the fluidized bed operated with different inlet gas velocities calculated with different drag models. (a) Ug = 0.05 m/s and (b) Ug = 0.15 m/s.

ANN-based fDEM drag reduced the mean error by 68.9% (from 4.70 to 1.46), 80.6%, and 74.7%, respectively. The fDEM-based results are better than fTFM-based results as expected. However, the errors predicted by the ANN-based model are slightly larger than those predicted by the NLR-based model. As shown in Figures 5 and 7, the heterogeneous index calculated from the NLR model is smoother than that calculated from the ANN model and the ANN model using linear interpolation in the dense regions. The potential overfit of the ANN model is low as the same R^2 values in both the training data set and the testing data set are observed. The computation wall time of the simulation with the ANN model is about 1.48 (CGR = 2) to 1.87 (CGR = 4) times of that with the NLR model. The poor performance may be because of the large size of the network used in this research. In a recent research[32] of the ANN regressed EMMS drag model, the computation wall time is about 1.21 times of the traditional method using a smaller ANN of three hidden layers with 32, 16, and 16 nodes in each layer. Further reduction of the ANN size leads to computation wall times similar to traditional methods. In that research, the simulations were performed with TFM and the ANN was directly implemented in user-defined functions. However, the direct utilization of the PyTorch library is more flexible as it can be easily extended to more complex networks if needed.

3.2. Filtered Drag from Bubbling Bed with Multiple Macroscale Velocities. In this section, the fluidized bed in Figure 3 was further simulated with gas inlet velocities of 0.05,

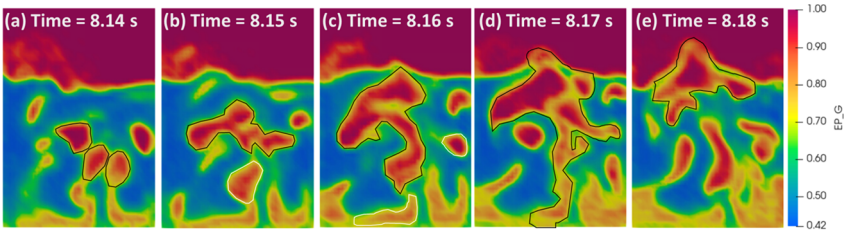

Figure 12. Evolution of bubbles in the fluidized bed operated with a velocity of 0.05 m/s. (a) Time = 8.14, (b) 8.15, (c) 8.16, (d) 8.17, and (e) 8.18 s.

https://doi.org/10.1021/acs.iecr.1c03644
Ind. Eng. Chem. Res. 2022, 61, 882−893

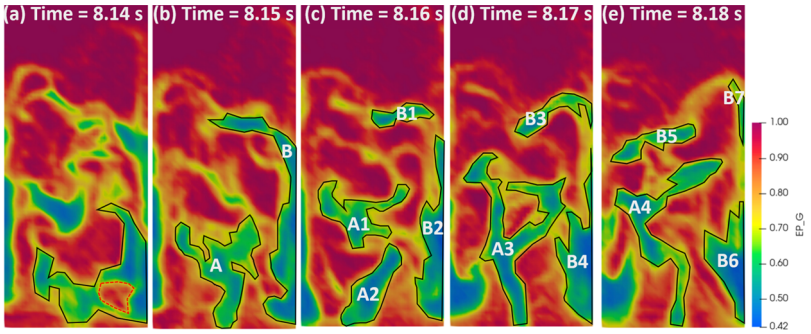

Figure 13. Evolution of clusters in the fluidized bed operated with a velocity of 0.15 m/s. (a) Time = 8.14, (b) 8.15, (c) 8.16, (d) 8.17, and (e) 8.18 s.

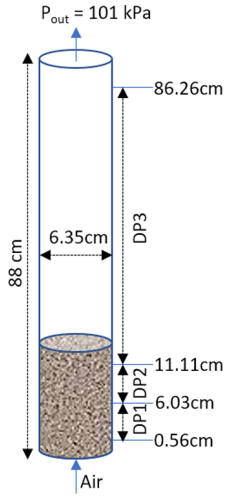

Figure 14. Dimensions of the simulated fluidized bed and main simulation parameters.

Table 2. Particle Properties and Parameters in the Simulations

properties/parameters	value
particle diameter (mm)	0.081
particle density (kg/m^3)	2493
spring constant (N/m)	200
restitution coefficient (−)	0.9
friction coefficient (−)	0.3
inlet gas velocity (cm/s)	7.28, 15.79
solid inventory (kg)	0.670
CFD grid length (cm)	6.35/32, 6.35/20, 6.35/16
coarse-graining ratio	12, 15

0.075, 0.125, and 0.15 m/s. Together with previous simulation results at 0.10 m/s, the influences of macroscale gas inlet velocities were analyzed. Similar to the previous section, the particle-scale heterogeneous indexes were grouped into bins based on the filtered voidage and dimensionless slip velocity. The voidages from 0.4 to 1.0 were equally divided into 60 bins, and the dimensionless slip velocities from 0.0 to 4.0 were equally divided into 50 bins.

3.2.1. Regression with Multiscale Markers. As shown in eq 24, an additional term χ is added to the previous nonlinear regression model to address the influence of macroscale gas inlet velocities. It is regressed with five additional parameters as a function of the filter size, voidage, dimensionless slip velocity, and dimensionless macroscale gas inlet velocity.

$$H_d = \begin{cases} 2 - 1.99(1 - e^{-\alpha(u_{\text{slip}}^* - u_0)^p}) + \chi, & u_{\text{slip}}^* > u_0 \\ 1, & u_{\text{slip}}^* \le u_0,\ \alpha_s > 0.59,\ \alpha_s < 0.01 \end{cases}$$

$$\chi = a_{21} + (a_{22} + a_{23}\Delta_{\text{filter}}^* + a_{24}\alpha_s + a_{25}u_{\text{slip}}^*)U_g/u_t \tag{25}$$

The regressed values of these coefficients are

$$\begin{aligned} a_{1-25} = [&4.802706, -12.753237, 67.982539, \\ &-96.535179, 104.148042, 0.014874, -0.200902, \\ &-0.00102, 0.038998, -1.492272, \\ &-0.317903, 0.121642, -0.024993, 0.155943, \\ &4.673687, 18.12709, 0.016406, -0.248029, \\ &-707.455212, 5.49012, 0.086153, 0.614471, \\ &-0.174122, -0.546865, -0.170773] \end{aligned}$$

The true values and the nonlinear regression predicted values of the heterogeneous index are compared in Figure 10. The R^2 value of 0.97 indicates a good regression of the model. Thus, there is no need to further explore ANN regression as the previous result already proved that the accuracy of the traditional NLR model is comparable or even better than that of the ANN-based model as long as it can regress the heterogeneous index with high accuracy. The reason is that these different regression models are only working as a numerical model to provide a correction value given an input condition.

3.2.2. Test of the Regressed Model. The regressed model was tested in the simulation of the fluidized beds with inlet gas velocities of 0.05 and 0.15 m/s. The errors in simulations using the drag model with the gas inlet velocity as an additional marker (blue line with squares in Figure 11) are reduced by 55.3 and 19.5%, respectively.

The macroscale condition such as the gas velocity in the bubbling fluidized bed dominates the evolution of mesoscale structures such as the generation, merging, rising, and breaking of the bubbles. Figure 12 shows the evolution of bubbles in the fluidized bed operated with a velocity of 0.05 m/s. From time 8.14 to 8.15 s, three small bubbles, outlined with black lines in Figure 12a, are merged into a big bubble as shown in Figure 12b. Then, it moves upward slowly due to the resistance of the particles above it. The small bubble below it, outlined with white lines in Figure 12b, moves up faster and merged with it at time 8.16 s. Several similar merges happened at time 8.17 s, and the

https://doi.org/10.1021/acs.iecr.1c03644
Ind. Eng. Chem. Res. 2022, 61, 882−893

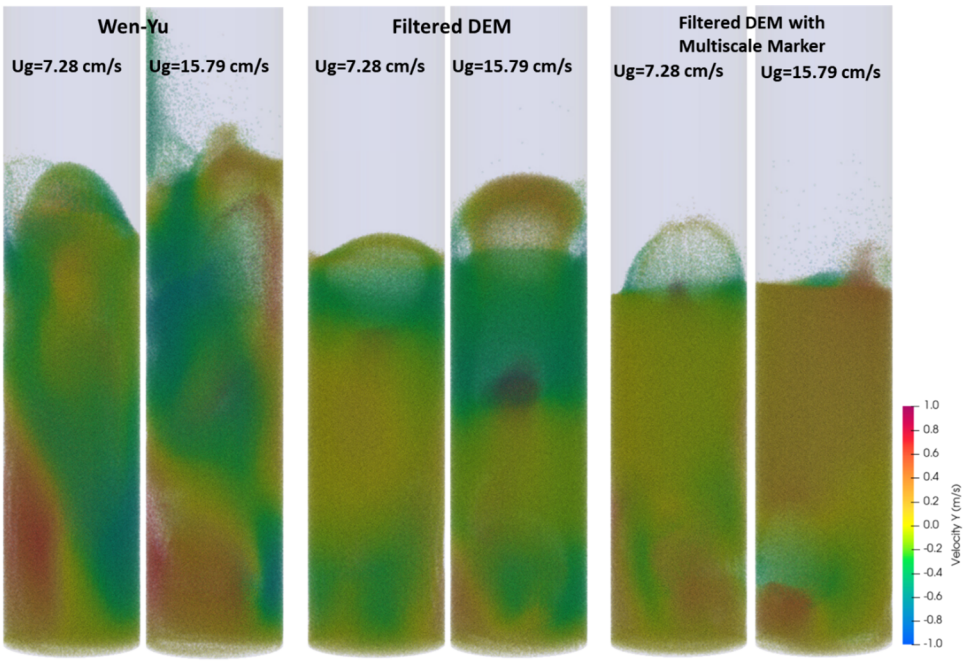

Figure 15. Particle distributions under different gas velocities simulated with different drag models using a coarse-graining ratio of 12.

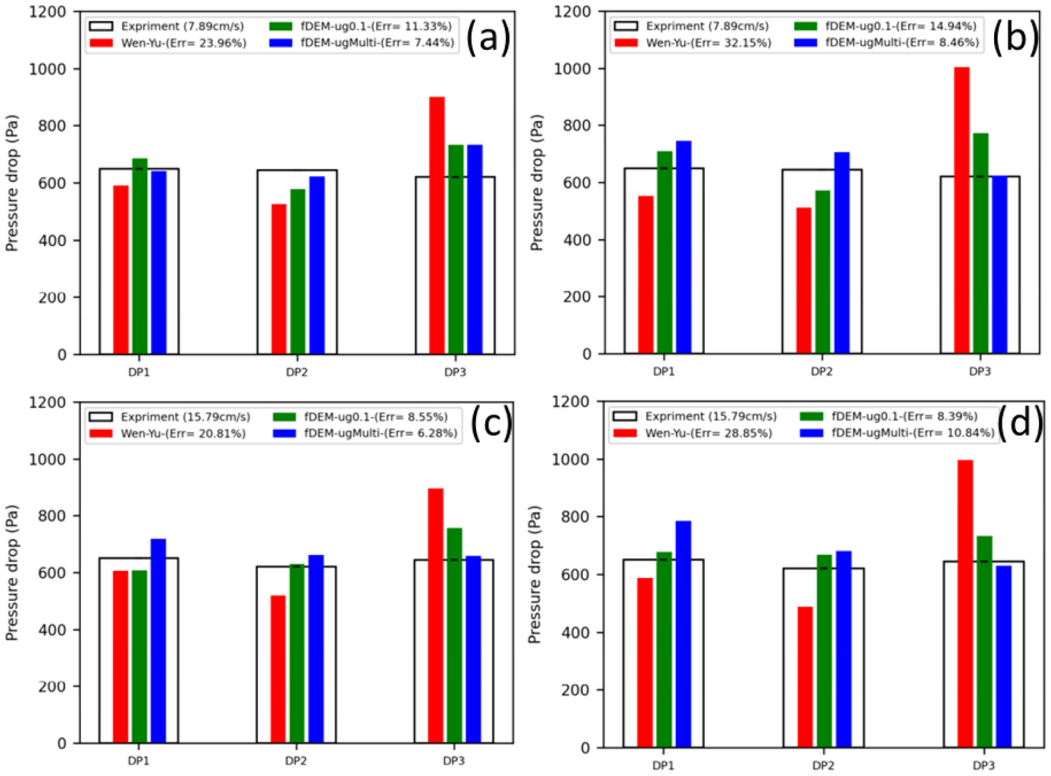

Figure 16. Pressure drops calculated with different drag models (red: Wen−Yu, green: filtered DEM, blue: filtered DEM with inlet velocity). (a): Gas velocity (Ug) equals 7.89 cm/s; coarse-graining ratio (CGR) equals 12. (b): Ug = 7.89 cm/s, CGR = 15. (c) Ug = 15.79 cm/s, CGR = 12. (d) Ug = 15.79 cm/s, CGR = 15

big bubble touches the freeboard of the bed and breaks up at time 8.18 s.

When the fluidized bed is operated under a gas velocity of 0.15 m/s, as shown in Figure 13, the hydrodynamics in the bed are dominated by the evolution of clusters rather than bubbles. From time 8.14 to 8.15 s, a bubble, outlined with red dash lines in Figure 13a, breaks a large cluster into two clusters: cluster A and cluster B. After 0.01 s, cluster A further breaks into cluster A1 and cluster A2, while cluster B breaks into cluster B1 and cluster B2 as shown in Figure 13c. From time 8.16 to 8.17 s, cluster A1 and cluster A2 merged into cluster A3, while cluster B1 and cluster B2 evolve into cluster B3 and cluster B4. After 0.01 s, cluster B3 breaks into cluster B5 and cluster B7. These dynamic evolutions of clusters dramatically changed the flow

https://doi.org/10.1021/acs.iecr.1c03644
Ind. Eng. Chem. Res. 2022, 61, 882−893

resistance at different locations and led to different gas flow patterns.

The significant difference of the mesoscale structures in the same fluidized bed operated with different gas velocities leads to different drag corrections as these structures are the origins of the need for subgrid corrections. This is why the errors can be reduced by up to 55.3% when the macroscale gas velocity is used as an additional marker in the derivation of the filtered drag models.

3.3. Application of the Filtered Drag. The derived drag model was tested in the simulation of a bubbling fluidized bed operated with Geldart A particles with a Sauter mean diameter of 0.081 mm and 2493 kg/m^3. As shown in Figure 14, four sensors are installed along the height of the bed to measure the pressure drops at three sections with a frequency of 100 Hz. A detailed experiment setup is available in the literature.[61] This fluidized bed operated under two different gas velocities was simulated with two different coarse-graining ratios using three different drag models. The simulation parameters are summarized in Table 2.

The particle distributions under different gas velocities simulated with different drag models using a coarse-graining ratio of 12 are shown in Figure 15. The Wen−Yu drag model predicted higher bed heights compared with the filtered drag models. The filtered drag with multiscale markers predicted slightly lower bed heights compared with the filtered drag with only mesoscale drag markers.

The accuracy of these simulations was further quantified using the experiment measured pressure drops as the benchmark. As shown in Figure 16, the Wen−Yu drag significantly overpredicted the pressure drop at DP3. The average error in these four cases using the Wen−Yu drag is 26.44%. The filtered drag without inlet gas velocity as an additional marker slightly overpredicted the pressure drop at DP3, and the average error is 10.80%. The simulation using the filtered drag with inlet gas velocity marker predicted the most accurate results with an average error of 8.26%. The error is reduced by 23.52%.

4. CONCLUSIONS

In this research, a filtered drag model was derived using data generated by fine-grid CFD-DEM simulations. The traditional nonlinear regression method was compared with the machine learning-based regression method using an Artificial Neural Network (ANN). The ANN model from PyTorch was then coupled with the MFiX software to conduct CFD simulations. The accuracy of the drag model was compared with the Wen−Yu drag model and a TFM derived filtered drag in the coarse-grained simulations of fluidized beds. The conclusions are as follows:

1) The filtered drag derived from CFD-DEM simulations is more accurate than the Wen−Yu drag and the filtered drag derived from TFM simulations.

2) The accuracy of the traditional nonlinear regression method derived drag model is slightly better than the ANN-based drag model. This is because the form of the nonlinear equations used in this research can fit the data with an R^2 value of 0.98, which is close to the ANN-based regression with an R^2 value of 0.99. The distribution of the heterogeneous index calculated from the traditional nonlinear regression model is smoother than that calculated from the ANN model.

3) The utilization of the gas inlet velocity as an additional macroscale marker reduced the errors by up to 55.3% in the tested cases. It demonstrated the importance of macroscale parameters in the derivation of mesoscale drag models. This multiscale approach was employed in the EMMS drag model but rarely investigated in the development of the filtered drag models.

The findings in this research may help the further development of the mesoscale drag model in several directions:

1) The traditional nonlinear regression method should not be blindly replaced with ANN as long as it can regress the data with high accuracy. However, the appropriate equation forms need more investigation. For ANN, the hyperparameters such as the number of layers and the number of nodes in each layer need further research for different problems.

2) The influence of other macroscale parameters such as reactor size and solid flux in the circulating fluidized beds may also be checked in the derivation of filtered drag models.

AUTHOR INFORMATION

Corresponding Author

Liqiang Lu − *National Energy Technology Laboratory, Morgantown, West Virginia 26507, United States; NETL Support Contractor, Morgantown, West Virginia 26507, United States;* orcid.org/0000-0002-5101-1688; Email: Liqiang.Lu@netl.doe.gov

Authors

Xi Gao − *Department of Chemical Engineering, Guangdong Technion-Israel Institute of Technology, Shantou, Guangdong 515063, China*

Jean-François Dietiker − *National Energy Technology Laboratory, Morgantown, West Virginia 26507, United States; NETL Support Contractor, Morgantown, West Virginia 26507, United States*

Mehrdad Shahnam − *National Energy Technology Laboratory, Morgantown, West Virginia 26507, United States*

William A. Rogers − *National Energy Technology Laboratory, Morgantown, West Virginia 26507, United States*

Complete contact information is available at: https://pubs.acs.org/10.1021/acs.iecr.1c03644

Notes

The authors declare no competing financial interest.

This project was funded by the United States Department of Energy, National Energy Technology Laboratory, in part, through a site support contract. Neither the United States Government nor any agency thereof, nor any of their employees, nor the support contractor, nor any of their employees, makes any warranty, express or implied, or assumes any legal liability or responsibility for the accuracy, completeness, or usefulness of any information, apparatus, product, or process disclosed, or represents that its use would not infringe privately owned rights. Reference herein to any specific commercial product, process, or service by trade name, trademark, manufacturer, or otherwise does not necessarily constitute or imply its endorsement, recommendation, or favoring by the United States Government or any agency thereof. The views and opinions of authors expressed herein do not necessarily state or reflect those of the United States Government or any agency thereof.

https://doi.org/10.1021/acs.iecr.1c03644
Ind. Eng. Chem. Res. 2022, 61, 882−893

REFERENCES

(1) Wang, S.; Luo, K.; Hu, C.; Sun, L.; Fan, J. Impact of Operating Parameters on Biomass Gasification in a Fluidized Bed Reactor: An Eulerian-Lagrangian Approach. *Powder Technol.* **2018**, *333*, 304−316.

(2) Hu, C.; Luo, K.; Wang, S.; Sun, L.; Fan, J. Computational Fluid Dynamics/Discrete Element Method Investigation on the Biomass Fast Pyrolysis: The Influences of Shrinkage Patterns and Operating Parameters. *Ind. Eng. Chem. Res.* **2019**, *58*, 1404−1416.

(3) Chen, X.-M.; Luo, Z.-H.; Zhu, Y.-P.; Xiao, J.; Chen, X. Direct Concurrent Multi-Scale CFD Modeling: The Effect of Intraparticle Transfer on the Flow Field in a MTO FBR. *Chem. Eng. Sci.* **2013**, *104*, 690−700.

(4) Zhu, L.-T.; Xie, L.; Xiao, J.; Luo, Z.-H. Filtered Model for the Cold-Model Gas−Solid Flow in a Large-Scale MTO Fluidized Bed Reactor. *Chem. Eng. Sci.* **2016**, *143*, 369−383.

(5) Liu, X.; Xu, J.; Ge, W.; Lu, B.; Wang, W. Long-Time Simulation of Catalytic MTO Reaction in a Fluidized Bed Reactor with a Coarse-Grained Discrete Particle Method — EMMS-DPM. *Chem. Eng. J.* **2020**, *389*, 124135.

(6) Hu, C.; Luo, K.; Wang, S.; Sun, L.; Fan, J. Influences of Operating Parameters on the Fluidized Bed Coal Gasification Process: A Coarse-Grained CFD-DEM Study. *Chem. Eng. Sci.* **2019**, *195*, 693−706.

(7) Cocco, R.; Karri, S. R.; Knowlton, T. Introduction to Fluidization. *Chem. Eng. Prog.* **2014**, *110*, 21.

(8) Singh, B. K.; Roy, S.; Buwa, V. V. Bubbling/Slugging Flow Behavior in a Cylindrical Fluidized Bed: ECT Measurements and Two-Fluid Simulations. *Chem. Eng. J.* **2020**, *383*, 123120.

(9) Wang, C.; Li, C.; Lan, X.; Wu, Y.; Gao, J. Particle Clustering (Mesoscale Structure) of High-Flux Gas−Solid Circulating Fluidized Bed. *Particuology* **2020**, *48*, 144−159.

(10) Wang, J.; van der Hoef, M. A.; Kuipers, J. A. M. Why the Two-Fluid Model Fails to Predict the Bed Expansion Characteristics of Geldart A Particles in Gas-Fluidized Beds: A Tentative Answer. *Chem. Eng. Sci.* **2009**, *64*, 622−625.

(11) Zhang, K.; Wang, S.; He, Y. Bubble-Induced Mesoscale Drag Model for the Simulation of Gas-Solid Bubbling Fluidization. *Chem. Eng. Sci.* **2021**, *246*, 116990.

(12) Ahmad, N.; Tong, Y.; Lu, B.; Wang, W. Extending the EMMS-Bubbling Model to Fluidization of Binary Particle Mixture: Parameter Analysis and Model Validation. *Chem. Eng. Sci.* **2019**, *200*, 257−267.

(13) Nikolopoulos, A.; Papafotiou, D.; Nikolopoulos, N.; Grammelis, P.; Kakaras, E. An Advanced EMMS Scheme for the Prediction of Drag Coefficient under a 1.2 MWth CFBC Isothermal Flow—Part I: Numerical Formulation. *Chem. Eng. Sci.* **2010**, *65*, 4080−4088.

(14) Yu, J.; Gao, X.; Lu, L.; Xu, Y.; Li, C.; Li, T.; Rogers, W. A. Validation of a Filtered Drag Model for Solid Residence Time Distribution (RTD) Prediction in a Pilot-Scale FCC Riser. *Powder Technol.* **2021**, *378*, 339−347.

(15) Sundaresan, S.; Ozel, A.; Kolehmainen, J. Toward Constitutive Models for Momentum, Species, and Energy Transport in Gas−Particle Flows. *Annu. Rev. Chem. Biomol. Eng.* **2018**, *9*, 61−81.

(16) Wang, W.; Lu, B.; Geng, J.; Li, F. Mesoscale Drag Modeling: A Critical Review. *Curr. Opin. Chem. Eng.* **2020**, *29*, 96−103.

(17) Schneiderbauer, S. A Spatially-Averaged Two-Fluid Model for Dense Large-Scale Gas-Solid Flows. *AIChE J.* **2017**, *63*, 3544−3562.

(18) Rauchenzauner, S.; Schneiderbauer, S. A Dynamic Anisotropic Spatially-Averaged Two-Fluid Model for Moderately Dense Gas-Particle Flows. *Int. J. Multiphase Flow* **2020**, *126*, 103237.

(19) Schneiderbauer, S. Validation Study on Spatially Averaged Two-Fluid Model for Gas−Solid Flows: I. A Priori Analysis of Wall Bounded Flows. *AIChE J.* **2018**, *64*, 1591−1605.

(20) Yang, N.; Wang, W.; Ge, W.; Li, J. CFD Simulation of Concurrent-up Gas−Solid Flow in Circulating Fluidized Beds with Structure-Dependent Drag Coefficient. *Chem. Eng. J.* **2003**, *96*, 71−80.

(21) Wang, W.; Li, J. Simulation of Gas−Solid Two-Phase Flow by a Multi-Scale CFD Approach—of the EMMS Model to the Sub-Grid Level. *Chem. Eng. Sci.* **2007**, *62*, 208−231.

(22) Lu, B.; Wang, W.; Li, J. Searching for a Mesh-Independent Sub-Grid Model for CFD Simulation of Gas−Solid Riser Flows. *Chem. Eng. Sci.* **2009**, *64*, 3437−3447.

(23) Wang, J.; Ge, W.; Li, J. Eulerian Simulation of Heterogeneous Gas−Solid Flows in CFB Risers: EMMS-Based Sub-Grid Scale Model with a Revised Cluster Description. *Chem. Eng. Sci.* **2008**, *63*, 1553−1571.

(24) Shi, Z.; Wang, W.; Li, J. A Bubble-Based EMMS Model for Gas−Solid Bubbling Fluidization. *Chem. Eng. Sci.* **2011**, *66*, 5541−5555.

(25) Hong, K.; Shi, Z.; Wang, W.; Li, J. A Structure-Dependent Multi-Fluid Model (SFM) for Heterogeneous Gas−Solid Flow. *Chem. Eng. Sci.* **2013**, *99*, 191−202.

(26) Luo, H.; Lu, B.; Zhang, J.; Wu, H.; Wang, W. A Grid-Independent EMMS/Bubbling Drag Model for Bubbling and Turbulent Fluidization. *Chem. Eng. J.* **2017**, *326*, 47−57.

(27) Zhou, Q.; Wang, J. CFD Study of Mixing and Segregation in CFB Risers: Extension of EMMS Drag Model to Binary Gas−Solid Flow. *Chem. Eng. Sci.* **2015**, *122*, 637−651.

(28) Li, F.; Song, F.; Benyahia, S.; Wang, W.; Li, J. MP-PIC Simulation of CFB Riser with EMMS-Based Drag Model. *Chem. Eng. Sci.* **2012**, *82*, 104−113.

(29) Lu, L.; Xu, J.; Ge, W.; Yue, Y.; Liu, X.; Li, J. EMMS-Based Discrete Particle Method (EMMS−DPM) for Simulation of Gas−Solid Flows. *Chem. Eng. Sci.* **2014**, *120*, 67−87.

(30) Jiang, Y.; Li, F.; Ge, W.; Wang, W. EMMS-Based Solid Stress Model for the Multiphase Particle-in-Cell Method. *Powder Technol.* **2020**, *360*, 1377−1387.

(31) Nikolopoulos, A.; Samlis, C.; Zeneli, M.; Nikolopoulos, N.; Karellas, S.; Grammelis, P. Introducing an Artificial Neural Network Energy Minimization Multi-Scale Drag Scheme for Fluidized Particles. *Chem. Eng. Sci.* **2021**, *229*, 116013.

(32) Yang, Z.; Lu, B.; Wang, W. Coupling Artificial Neural Network with EMMS Drag for Simulation of Dense Fluidized Beds. *Chem. Eng. Sci.* **2021**, *246*, 117003.

(33) Igci, Y.; Andrews, A. T., IV; Sundaresan, S.; Pannala, S.; O'Brien, T. Filtered Two-Fluid Models for Fluidized Gas-Particle Suspensions. *AIChE J.* **2008**, *54*, 1431−1448.

(34) Igci, Y.; Sundaresan, S. Constitutive Models for Filtered Two-Fluid Models of Fluidized Gas−Particle Flows. *Ind. Eng. Chem. Res.* **2011**, *50*, 13190−13201.

(35) Milioli, C. C.; Milioli, F. E.; Holloway, W.; Agrawal, K.; Sundaresan, S. Filtered Two-Fluid Models of Fluidized Gas-Particle Flows: New Constitutive Relations. *AIChE J.* **2013**, *59*, 3265−3275.

(36) Sarkar, A.; Milioli, F. E.; Ozarkar, S.; Li, T.; Sun, X.; Sundaresan, S. Filtered Sub-Grid Constitutive Models for Fluidized Gas-Particle Flows Constructed from 3-D Simulations. *Chem. Eng. Sci.* **2016**, *152*, 443−456.

(37) Gao, X.; Li, T.; Sarkar, A.; Lu, L.; Rogers, W. A. Development and Validation of an Enhanced Filtered Drag Model for Simulating Gas-Solid Fluidization of Geldart A Particles in All Flow Regimes. *Chem. Eng. Sci.* **2018**, *184*, 33−51.

(38) Zhu, L.-T.; Liu, Y.-X.; Luo, Z.-H. An Effective Three-Marker Drag Model via Sub-Grid Modeling for Turbulent Fluidization. *Chem. Eng. Sci.* **2018**, *192*, 759−773.

(39) Zhu, L.-T.; Liu, Y.-X.; Tang, J.-X.; Luo, Z.-H. A Material-Property-Dependent Sub-Grid Drag Model for Coarse-Grained Simulation of 3D Large-Scale CFB Risers. *Chem. Eng. Sci.* **2019**, *204*, 228−245.

(40) Parmentier, J.-F.; Simonin, O.; Delsart, O. A Functional Subgrid Drift Velocity Model for Filtered Drag Prediction in Dense Fluidized Bed. *AIChE J.* **2012**, *58*, 1084−1098.

(41) Ozel, A.; Fede, P.; Simonin, O. Development of Filtered Euler−Euler Two-Phase Model for Circulating Fluidised Bed: High Resolution Simulation, Formulation and a Priori Analyses. *Int. J. Multiphase Flow* **2013**, *55*, 43−63.

(42) Jiang, M.; Chen, X.; Zhou, Q. A Gas Pressure Gradient-Dependent Subgrid Drift Velocity Model for Drag Prediction in Fluidized Gas−Particle Flows. *AIChE J.* **2020**, *66*, No. e16884.

https://doi.org/10.1021/acs.iecr.1c03644
Ind. Eng. Chem. Res. 2022, 61, 882−893

(43) Jiang, Y.; Kolehmainen, J.; Gu, Y.; Kevrekidis, Y. G.; Ozel, A.; Sundaresan, S. Neural-Network-Based Filtered Drag Model for Gas-Particle Flows. *Powder Technol.* **2019**, *346*, 403−413.
(44) Zhu, L.-T.; Tang, J.-X.; Luo, Z.-H. Machine Learning to Assist Filtered Two-Fluid Model Development for Dense Gas−Particle Flows. *AIChE J.* **2020**, *66*, No. e16973.
(45) Zhang, Y.; Jiang, M.; Chen, X.; Yu, Y.; Zhou, Q. Modeling of the Filtered Drag Force in Gas−Solid Flows via a Deep Learning Approach. *Chem. Eng. Sci.* **2020**, *225*, 115835.
(46) Jiang, Y.; Chen, X.; Kolehmainen, J.; Kevrekidis, I. G.; Ozel, A.; Sundaresan, S. Development of Data-Driven Filtered Drag Model for Industrial-Scale Fluidized Beds. *Chem. Eng. Sci.* **2021**, *230*, 116235.
(47) Milioli, C. C.; Milioli, F. E. On the Subgrid Behavior of Accelerated Riser Flows for a High Stokes Number Particulate. *Ind. Eng. Chem. Res.* **2011**, *50*, 13538−13544.
(48) Mouallem, J.; Niaki, S. R. A.; Chavez-Cussy, N.; Milioli, C. C.; Milioli, F. E. Macro-Scale Effects over Filtered and Residual Stresses in Gas-Solid Riser Flows. *Chem. Eng. Sci.* **2019**, *195*, 553−564.
(49) Lu, L.; Xu, Y.; Li, T.; Benyahia, S. Assessment of Different Coarse Graining Strategies to Simulate Polydisperse Gas-Solids Flow. *Chem. Eng. Sci.* **2018**, *179*, 53−63.
(50) Benyahia, S.; Sundaresan, S. Do We Need Sub-Grid Scale Corrections for Both Continuum and Discrete Gas-Particle Flow Models? *Powder Technol.* **2012**, *220*, 2−6.
(51) Ozel, A.; Kolehmainen, J.; Radl, S.; Sundaresan, S. Fluid and Particle Coarsening of Drag Force for Discrete-Parcel Approach. *Chem. Eng. Sci.* **2016**, *155*, 258−267.
(52) Lu, L.; Konan, A.; Benyahia, S. Influence of Grid Resolution, Parcel Size and Drag Models on Bubbling Fluidized Bed Simulation. *Chem. Eng. J.* **2017**, *326*, 627−639.
(53) Radl, S.; Sundaresan, S. A Drag Model for Filtered Euler−Lagrange Simulations of Clustered Gas−Particle Suspensions. *Chem. Eng. Sci.* **2014**, *117*, 416−425.
(54) Yu, Y.; Li, Y.; Jiang, M.; Zhou, Q. Meso-Scale Drag Model Designed for Coarse-Grid Eulerian-Lagrangian Simulation of Gas-Solid Flows. *Chem. Eng. Sci.* **2020**, *223*, 115747.
(55) Lei, H.; Liao, J.-W.; Zhu, L.-T.; Luo, Z.-H. CFD-DEM Modeling of Filtered Fluid-Particle Drag and Heat Transfer in Bidisperse Gas-Solid Flows. *Chem. Eng. Sci.* **2021**, *246*, 116896.
(56) Xu, M.; Ge, W.; Li, J. A Discrete Particle Model for Particle−Fluid Flow with Considerations of Sub-Grid Structures. *Chem. Eng. Sci.* **2007**, *62*, 2302−2308.
(57) Lu, L.; Gao, X.; Li, T.; Benyahia, S. Numerical Investigation of the Ability of Salt Tracers to Represent the Residence Time Distribution of Fluidized Catalytic Cracking Particles. *Ind. Eng. Chem. Res.* **2017**, *56*, 13642−13653.
(58) Xie, J.; Zhong, W.; Yu, A. MP-PIC Modeling of CFB Risers with Homogeneous and Heterogeneous Drag Models. *Adv. Powder Technol.* **2018**, *29*, 2859−2871.
(59) Lu, L. GPU Accelerated MFiX-DEM Simulations of Granular and Multiphase Flows. *Particuology* **2022**, *62*, 14−24.
(60) Wen, C. Y.; Yu, Y. H. Mechanics of Fluidization. *Chem. Eng. Prog. Sym. Ser.* **1966**, *62*, 100−111.
(61) Vaidheeswaran, A.; Pandey, R.; Clarke, M. A.; Ashfaq, H.; Rogers, W. A. *Fluidization of Group A Glass Particles: Experiments and Preliminary Validation*; b9d9e6e7-56e4-42a1-9de2-d565514e3cb7; National Energy Technology Laboratory (NETL), Pittsburgh, PA, Morgantown, WV, and Albany, OR (United States), 2020, DOI: 10.2172/1632859.